The Astrophysical Journal, 866:39 (9pp), 2018 October 10 https://doi.org/10.3847/1538-4357/aadb8e

Gaia and the Galactic Center Origin of Hypervelocity Stars

Warren R. Brown[1], Mario G. Lattanzi[2], Scott J. Kenyon[1], and Margaret J. Geller[1]
[1] Smithsonian Astrophysical Observatory 60 Garden Street, Cambridge, MA 02138, USA; wbrown@cfa.harvard.edu
[2] Instituto Nazionale di Astrofisica—Osservatorio Astronomico di Torino Via Osservatorio 20, I-10025 Pino Torinese, Italy
Received 2018 May 10; revised 2018 August 3; accepted 2018 August 17; published 2018 October 8

Abstract

We use new *Gaia* measurements to explore the origin of the highest velocity stars in the hypervelocity star (HVS) survey. The measurements reveal a clear pattern in B-type stars. Halo stars dominate the sample at speeds of $\simeq$100 km s^{-1} below Galactic escape velocity. Disk runaway stars have speeds up to $\simeq$100 km s^{-1} above Galactic escape velocity, but most disk runaways are bound. Stars with speeds $\gtrsim$100 km s^{-1} above Galactic escape velocity originate from the Galactic center. Two bound stars may also originate from the Galactic center. Future *Gaia* measurements will enable a large, clean sample of Galactic center ejections for measuring the massive black hole ejection rate of HVSs, and for constraining the mass distribution of the Milky Way dark matter halo.

Key words: Galaxy: halo – Galaxy: kinematics and dynamics – stars: early-type – stars: kinematics and dynamics

1. Introduction

Hills (1988) first proposed that a three-body exchange between a pair of stars and a massive black hole (MBH) can eject "hypervelocity stars" (HVSs) at 1000 km s^{-1} velocities from the Galactic center. We discovered the first HVS (Brown et al. 2005). This 3 $M_\odot$ main-sequence B star moves with a Galactic rest frame velocity >670 km s^{-1}, about twice the Galactic escape velocity at its current distance of 100 kpc. Only a gravitational interaction with a massive compact object can plausibly explain its motion.

The discovery of HVS1 inspired the HVS Survey, a targeted radial velocity survey of B-type stars that should not exist at faint magnitudes in the halo (Brown et al. 2006, 2007b). Twenty-one stars are significantly unbound in radial velocity alone (Brown et al. 2014). The extreme velocities, the short-lived nature of the stars, their distribution in Galactic latitude, and their overall numbers match theoretical expectations for the Galactic center origin proposed by Hills (1988). However, the measurements provide only an indirect link to the MBH.

Alternative origins for unbound stars include ejection from the Galactic disk through binary disruption (Blaauw 1961; Poveda et al. 1967) and ejection from the Large Magellanic Cloud (Boubert & Evans 2016; Boubert et al. 2017). Galactic disk ejections are called "runaways" (Blaauw 1961; Greenstein & Sargent 1974). The disruption of a binary by a supernova, where the surviving star is released at the orbital velocity of the progenitor binary, can yield unbound runaways in extreme circumstances (e.g., Tauris 2015). The first example of an unbound main-sequence runaway is the B star HD 271791 (Heber et al. 2008; Przybilla et al. 2008b). The first example of an unbound Large Magellanic Cloud ejection is the B star HE 0437−5439 (Edelmann et al. 2005; Przybilla et al. 2008a; Erkal et al. 2018). Compact objects like white dwarfs can have higher binary disruption ejection velocities than main-sequence stars. The first observational examples are the unbound subdwarf O star US 708 (Hirsch et al. 2005; Justham et al. 2009; Wang & Han 2009; Geier et al. 2015), the white dwarf LP 40–365 (Vennes et al. 2017; Raddi et al. 2018), and three white dwarf candidates found with *Gaia* (Shen et al. 2018).

The European Space Agency mission *Gaia* has begun a new era of precision astrometry. The trajectories of unbound stars hold the key to their origin. Measuring radial velocity to km s^{-1} precision is easy with modern spectroscopy; measuring tangential velocity, the product of distance and proper motion, is difficult. Known HVSs are at distances of 50–100 kpc; their expected proper motions are <1 mas yr^{-1}. Newly released *Gaia* Data Release 2 provides improved proper motions for many HVSs (Gaia Collaboration et al. 2018a). Here, we use *Gaia* measurements to determine the origin of stars from the HVS Survey (Brown et al. 2007b, 2014) on the basis of their trajectory and velocity.

In Section 2, we define the sample and compare *Gaia* proper motions with previous *Hubble Space Telescope* (*HST*) measurements. In Section 3, we evaluate the origin of these stars on the basis of computed trajectories and ejection velocities. The results are in Section 4, and we conclude in Section 5. We identify Galactic center HVSs, Galactic disk runaways, and Galactic halo stars with different but overlapping velocities; the highest velocity stars are probably Galactic center ejections.

2. Data

2.1. Sample

We study 42 radial velocity outliers from the HVS Survey (Brown et al. 2007b, 2014). We include all stars with heliocentric radial velocity transformed to the Galactic frame $v_{\rm rf} > +275$ km s^{-1},

$$v_{\rm rf} = v_{\rm helio} + 11.1 \cos l \cos b + 247.24 \sin l \cos b + 7.25 \sin b, \quad (1)$$

where l and b are Galactic longitude and latitude, respectively, and we assume that the Sun is moving with respect to the local standard of rest as measured by Schönrich et al. (2010) and the Galactic disk circular velocity is 235 km s^{-1} (Reid et al. 2014). We choose $v_{\rm rf} > +275$ km s^{-1} because of the significant absence of negative velocity outliers in the HVS Survey. The four most negative velocity stars have $-300 < v_{\rm rf} < -275$ km s^{-1} (Brown et al. 2014), implying that the 42 stars with $v_{\rm rf} > +275$ km s^{-1} are a relatively clean sample of ejected stars with minimal halo star contamination.

The HVS Survey targeted stars selected by color (Brown et al. 2012) with no kinematic selection. The spectroscopy is 99% complete. Stellar atmosphere fits establish that the majority of

Table 1
HVS Survey Stars with $v_{rf} > +275$ km s^{-1}, Ordered by v_{rf}

ID	R.A. (J2000)	Decl. (J2000)	g (mag)	*Gaia* (μ_α, μ_δ) (mas yr^{-1}, mas yr^{-1})	*HST* (μ_α, μ_δ) (mas yr^{-1}, mas yr^{-1})	GPS1 (μ_α, μ_δ) (mas yr^{-1}, mas yr^{-1})
HVS1	9:07:45.0	2:45:07	19.79	−1.012 ± 1.321, −0.269 ± 0.879	0.080 ± 0.261, −0.117 ± 0.221	...
HVS5	9:17:59.5	67:22:38	17.93	0.017 ± 0.176, −1.164 ± 0.268	0.554 ± 0.615, −0.438 ± 0.589	−1.265 ± 2.248, 3.747 ± 1.837
HVS4	9:13:01.0	30:51:20	18.40	−0.308 ± 0.647, −1.055 ± 0.481	−0.230 ± 0.362, −0.422 ± 0.358	−1.378 ± 2.128, 2.240 ± 1.651
HVS6	11:05:57.5	9:34:39	19.06	−0.367 ± 0.664, −0.694 ± 0.507	0.051 ± 0.568, 0.307 ± 0.967	2.791 ± 1.773, 2.488 ± 2.369
HVS19	11:35:17.8	8:02:01	20.18	−0.626 ± 1.790, 0.363 ± 1.224	...	...
HVS22	11:41:46.4	4:42:17	20.26	0.180 ± 2.024, 1.964 ± 1.443	...	...
HVS9	10:21:37.1	−0:52:35	18.84	0.345 ± 0.743, −0.117 ± 0.747	−1.260 ± 0.736, −0.250 ± 0.697	0.212 ± 1.427, 0.439 ± 1.393
HVS18	23:29:04.9	33:00:11	19.66	−0.308 ± 0.656, −0.157 ± 0.495	...	−4.434 ± 2.749, 5.957 ± 3.858
B733	14:49:55.6	31:03:51	15.75	−1.231 ± 0.060, −4.547 ± 0.094	−1.769 ± 0.939, −3.709 ± 1.017	1.425 ± 1.276, −1.627 ± 1.102
HVS17	16:41:56.4	47:23:46	17.50	−1.069 ± 0.198, −1.104 ± 0.323	...	0.615 ± 1.763, 0.314 ± 1.551
HVS13	10:52:48.3	−0:01:34	20.18	−0.729 ± 1.949, 0.047 ± 1.345	−0.898 ± 0.385, 0.456 ± 0.439	...
HVS12	10:50:09.6	3:15:51	19.77	0.425 ± 1.377, 0.193 ± 0.993	−0.404 ± 0.364, 0.314 ± 0.337	−3.040 ± 2.368, −0.678 ± 2.408
HVS10	12:03:37.9	18:02:50	19.30	−3.161 ± 1.288, −1.149 ± 0.494	−1.075 ± 0.362, −0.583 ± 0.419	3.292 ± 2.459, 0.702 ± 1.933
HVS8	9:42:14.0	20:03:22	18.05	−0.805 ± 0.365, −0.055 ± 0.369	−0.821 ± 1.261, −0.039 ± 0.697	3.217 ± 2.425, −0.251 ± 2.582
HVS7	11:33:12.1	1:08:25	17.75	−0.701 ± 0.373, 0.412 ± 0.253	0.996 ± 0.961, −0.549 ± 1.158	−4.776 ± 1.377, 0.717 ± 1.440
HVS20	11:36:37.1	3:31:07	19.89	0.458 ± 1.451, 0.574 ± 1.014	...	...
HVS21	10:34:18.3	48:11:35	19.78	0.003 ± 0.693, −0.224 ± 0.881	...	...
B485	10:10:18.8	30:20:28	16.16	−0.789 ± 0.131, −0.141 ± 0.127	−1.665 ± 0.722, −1.149 ± 0.628	−0.820 ± 2.048, −0.802 ± 1.977
HVS24	11:11:36.4	0:58:56	18.98	0.292 ± 0.777, −0.379 ± 0.578	...	−4.431 ± 2.916, −1.653 ± 3.129
HVS16	12:25:23.4	5:22:34	19.40	−1.643 ± 1.518, −1.101 ± 0.856	...	1.742 ± 2.090, −2.240 ± 1.903
B1080	10:33:57.3	−1:15:07	18.73	−0.957 ± 0.599, −0.619 ± 0.417	...	...
HVS15	11:33:41.1	−1:21:14	19.24	−0.888 ± 1.291, −0.316 ± 0.567	...	−2.524 ± 1.783, −4.246 ± 1.778
B1085	11:22:55.8	−9:47:35	17.53	−2.251 ± 0.246, −0.333 ± 0.172	...	2.116 ± 2.201, −3.046 ± 1.861
B434	11:02:24.4	2:50:03	18.15	0.095 ± 0.375, −1.954 ± 0.300	−1.613 ± 0.575, −0.264 ± 0.650	1.006 ± 1.656, −1.559 ± 1.644
B537	0:28:10.3	21:58:10	17.35	0.761 ± 0.229, −0.506 ± 0.120	...	...
B080	11:06:28.2	−8:22:48	18.68	−0.186 ± 0.537, 0.060 ± 0.415	...	−2.575 ± 3.455, −4.762 ± 2.080
B572	0:59:56.1	31:34:39	18.02	0.488 ± 0.329, −−0.989 ± 0.366	...	−1.850 ± 4.124, 2.423 ± 1.393
B458	10:43:18.3	−1:35:03	19.44	0.652 ± 0.892, −0.197 ± 0.747	...	−0.276 ± 1.559, −2.714 ± 1.648
B711	14:20:01.9	12:44:05	17.00	0.594 ± 0.209, −2.582 ± 0.172	−0.960 ± 0.942, 1.545 ± 0.999	2.790 ± 1.527, 0.636 ± 1.140
B576	14:04:32.4	35:22:58	17.53	−3.201 ± 0.130, −0.957 ± 0.129	...	3.199 ± 1.354, 0.729 ± 1.379
B095	10:13:59.8	56:31:12	19.86	−0.319 ± 0.854, 0.769 ± 0.864	...	1.972 ± 2.280, 0.282 ± 1.693
B495	11:52:45.9	−2:11:16	18.22	−0.124 ± 0.505, 0.164 ± 0.227	...	−0.604 ± 1.648, 0.621 ± 1.325
B1139	18:00:50.9	48:24:25	17.66	−1.351 ± 0.192, −1.032 ± 0.214	...	−0.843 ± 1.132, 0.216 ± 1.235
B598	14:17:23.3	10:12:46	18.49	−1.925 ± 0.583, −0.820 ± 0.526	...	−1.156 ± 2.400, −2.482 ± 2.407
B329	15:48:06.9	9:34:24	19.05	−1.321 ± 0.603, −0.983 ± 0.583	...	−0.367 ± 2.016, −3.864 ± 1.859
B129	7:49:50.2	24:38:41	18.63	0.697 ± 0.583, −0.680 ± 0.432	...	0.548 ± 1.391, −1.619 ± 1.486
B143	8:18:28.1	57:09:22	17.55	0.381 ± 0.207, −1.490 ± 0.180	...	4.820 ± 1.740, 2.803 ± 1.555
B481	23:22:29.5	4:36:51	17.63	2.027 ± 0.322, −1.321 ± 0.209	...	−1.861 ± 1.506, 0.834 ± 1.475
B167	9:07:10.1	36:59:58	18.16	−0.630 ± 0.310, −0.178 ± 0.293	...	2.015 ± 1.809, −0.537 ± 1.497

unbound stars are main-sequence B stars (Brown et al. 2014, 2015, and references therein). The bound stars are also probably main-sequence B stars on the basis of their velocity distribution. The absence of −300 km s^{-1} stars in the HVS Survey implies that the +300 km s^{-1} stars must have lifetimes less than their ∼1 Gyr orbital turn-around time (Brown et al. 2007a; Kollmeier & Gould 2007; Yu & Madau 2007). Thus they are B stars, and we calculate stellar distances using Padova main-sequence tracks (Girardi et al. 2004; Marigo et al. 2008; Bressan et al. 2012) with an estimated precision of 15%. We transform heliocentric distances to the Galactic frame assuming that the Sun is located 8 kpc from the Galactic center (Camarillo et al. 2018).

The HVS Survey exclusively samples the stellar halo. The $17 < g < 20.25$ apparent magnitude limit corresponds to approximately $30 < R < 120$ kpc in Galactocentric radial distance. For completeness, we include five stars from the bright $15 < g < 19.5$ portion of the initial HVS Survey (Brown et al. 2007b). The bright stars are nearby $10 < R < 30$ kpc and bound, but four have *HST* proper motion measurements for comparison with *Gaia*.

Table 1 lists the sample of 42 stars with their coordinates and apparent g-band SDSS magnitude. We sort the table by decreasing v_{rf}. We refer to bound objects with the letter B followed by their target number in the HVS Survey, and unbound objects by their published HVS number. We also list the east–west and north–south components of proper motion, (μ_α, μ_δ), obtained from three sources.

2.2. Proper Motions

Gaia Data Release 2 contains proper motions for 39 of the 42 stars listed in Table 1. The three missing stars (HVS14, HVS23, and B149) have too few *Gaia* measurements for a robust solution. We drop them from further consideration. The remaining 39 velocity outliers satisfy the quality controls recommended by Lindegren et al. (2018): i.e., the objects all have >10 visibility periods, <1.4 mas astrometric excess noise, and the longest semimajor axis in the five-dimensional error ellipses is <1.9 mas. For reference, the median *Gaia* proper motion error for the 39 objects is ±0.73 mas yr^{-1}. The brightest stars have errors of only ±0.11 mas yr^{-1}.

2.2.1. Gaia *Covariances*

Because *Gaia* values are derived from a five-parameter astrometric solution (Lindegren et al. 2018), the *Gaia* proper motions are correlated with our choice of parallax = 1/distance. We simplify the issue by assuming that position errors are zero. The remaining three covariances are between parallax and the two components of proper motion.

In practice, *Gaia* parallax errors provide so little constraint that the covariances affect our results very little. *Gaia* parallaxes for our sample range from −1.06 mas to +1.20 mas, with a mean of -0.011 ± 0.43 mas. The mean spectrophotometric parallax in our sample, 0.02 ± 0.003 mas, is 100 times more precise. The typical 0.5σ difference between the *Gaia* parallax and our spectrophotometric parallax yields a typical 0.055 mas yr^{-1} shift in the *Gaia* proper motion value, a shift that is about 10% of the published proper motion error. Physically, this shift corresponds to a 13 km s^{-1} ($\simeq$10%) change in tangential velocity, and an even smaller change to the total velocity of the stars.

Table 1 lists the *Gaia* proper motion values appropriate for our adopted distances.

2.2.2. *HST* Comparison

Brown et al. (2015) publish independent proper motion measurements made with *HST* for 14 stars. The *HST* proper motions were measured relative to background galaxies. They thus provide a test of *Gaia*'s absolute reference frame.

Figure 1 (upper panel) plots the difference between *Gaia* and *HST* proper motion divided by the errors summed in quadrature. Clipping two $>3\sigma$ outliers (see below), the average difference $\Delta\mu_\alpha(Gaia - HST) = -0.16 \pm 0.31$ mas yr^{-1} and $\Delta\mu_\delta(Gaia - HST) = -0.20 \pm 0.25$ mas yr^{-1} consistent with zero.

The comparison also reveals that the most problematic *HST* measurements are the brightest stars. For bright stars, Brown et al. (2015) paired short and long exposures to tie the stars to faint background galaxies. This approach likely introduced additional errors. We add ±0.5 mas yr^{-1} in quadrature to the published *HST* error for those objects (B434, B485, B711, B711, HVS7, HVS8). The median *HST* proper motion error for the 14 stars is then ±0.91 mas yr^{-1}; the best-measured star has an error of ±0.34 mas yr^{-1}.

The *HST* measurements highlight the value of obtaining pointed observations with long exposure times. Although *Gaia* errors are three times better than *HST* errors for bright stars, *HST* errors are four times better than *Gaia* errors for faint stars like HVS1. Errors are comparable in size at $g \simeq 18.5$ mag. A weighted mean would maximize the information from *HST* and *Gaia*; however, we do not want to add measurements that include possible systematic errors.

We adopt *Gaia* proper motions for the seven bright $g < 18$ stars with $\sigma_{HST} > 2\sigma_{Gaia}$. This subset includes all stars observed with paired short+long exposures in the *HST* program. We adopt a weighted mean for the three $18 < g < 19$ stars where σ_{HST} and σ_{Gaia} are within a factor of two (HVS4, HVS6, and HVS9). We adopt the *HST* proper motions for the four $g > 19$ stars with $\sigma_{Gaia} > 2\sigma_{HST}$ (HVS1, HVS10, HVS12, HVS13).

2.2.3. *GPS1* Comparison

We compare *Gaia* proper motions with the *Gaia*-PanStarrs1-SDSS catalog (GPS1, Tian et al. 2017). GPS1 proper motions are based on astrometric positions from ground-based PanStarrs1, SDSS, and 2MASS catalogs plus *Gaia* Data Release 1. Because the GPS1 time baseline comes from the ground-based catalogs, and because *Gaia* Data Release 2 is a new solution to the *Gaia* measurements, GPS1 proper motions are essentially independent of *Gaia* Data Release 2 values. GPS1 proper motions are available for 33 stars.

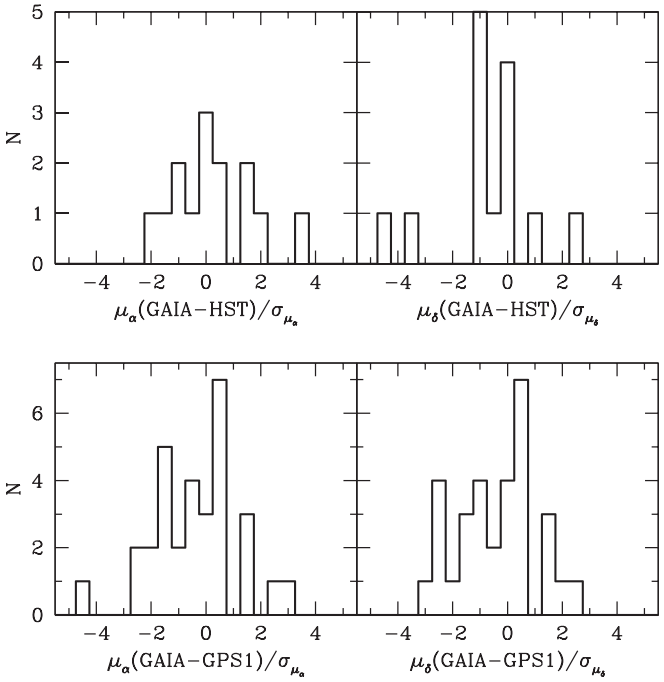

Figure 1. Difference between *Gaia* and *HST* proper motions (upper panel) or GPS1 proper motions (lower panel), divided by the errors summed in quadrature. Left-hand panels plot east–west (μ_α) differences; right-hand panels plot north–south (μ_δ) differences. The mean differences are consistent with zero, but the comparison finds notable outliers.

Figure 1 (lower panel) plots the difference between *Gaia* and *GPS1* proper motion divided by the errors summed in quadrature. Clipping two $>3\sigma$ outliers, the average difference $\Delta\mu_{\rm R.A.}(Gaia - \text{GPS1}) = -0.18 \pm 0.40$ mas yr^{-1} and $\Delta\mu_{\rm Decl.}(Gaia - \text{GPS1}) = -0.38 \pm 0.35$ mas yr^{-1} consistent with zero. The distribution in declination shows a possible asymmetry.

Despite the longer time baseline of ground-based observations, $\sigma_{\rm GPS1} \simeq 5\sigma_{Gaia}$. Thus we do not use GPS1 values here. The median GPS1 proper motion error for the 33 stars is ±2.69 mas yr^{-1}; the best-measured star has an error of ±1.68 mas yr^{-1}.

3. Analysis

We evaluate the probability of origin on the basis of computed trajectories and ejection velocities. We select a gravitational potential model, trace the trajectory of each star backwards in time, and calculate the required ejection velocity from that position in the Milky Way. We estimate likelihood from the density distribution of simulated trajectories as they cross the Galactic plane.

3.1. Gravitational Potential Model

To address the origin of HVS ejections from the Galactic center, we require a gravitational potential model that fits observed mass measurements from the Galactic center to the outer halo. We adopt

the three-component bugle–disk–halo model of Kenyon et al. (2014). The model has a flat 235 km s^{-1} rotation curve and a 10^{12} $M_\odot$ halo mass consistent with recent *Gaia* measurements from the orbits of globular clusters and dwarf galaxies (Fritz et al. 2018; Gaia Collaboration et al. 2018b; Posti & Helmi 2018; Watkins et al. 2018).

The results are insensitive to the choice of potential model because the stars are on nearly radial trajectories. Inserting a simulated 10^{11} $M_\odot$ Large Magellanic Cloud into the potential model (see Kenyon et al. 2018) changes the computed flight times by <1 Myr, changes the Galactic plane crossing location of the orbits by <0.4 kpc, and changes the effective escape velocity by <10 km s^{-1}. We thus choose to work with the three-component model.

We determine effective Galactic escape velocity, $v_{\rm esc}$, by dropping a test particle from rest at the virial radius. At the solar circle $R = 8$ kpc, $v_{\rm esc} = 580$ km s^{-1} consistent with the most recent solar neighborhood escape velocity measurement (Monari et al. 2018). At the radius of influence of the supermassive black hole, $v_{\rm esc} \geqslant 900$ km s^{-1} (Kenyon et al. 2008). Only a gravitational interaction with the supermassive black hole can eject a main-sequence star at >900 km s^{-1} (Hills 1988). At the median $R = 55$ kpc depth of the HVS Survey sample, $v_{\rm esc} = 350$ km s^{-1}.

3.2. Trajectory Calculation

Calculations are straightforward for the nearly radial trajectories of the stars. We start from the measured position and velocity of each star, and integrate its trajectory backward in time through the Galactic potential. We record where each trajectory crosses the Galactic plane, and its distance from the Galactic center. We also record the ejection velocity required to launch the star from the disk-crossing location, given the angle of the trajectory relative to Galactic rotation.

Figure 2 plots the proper motion measurement for each star. Because we know position and radial velocity, a proper motion in Figure 2 corresponds to a unique trajectory through the Galaxy given a gravitational potential model. The blue ellipses in Figure 2 are the loci of proper motions with trajectories that cross the Galactic plane at $R = 20$ kpc, the edge of the Milky Way disk. The red circle is the region of minimum Galactic disk ejection velocity, the region where Galactic disk ejections can most easily escape the gravitational pull of the Milky Way. A Galactic center trajectory is marked by the large black dot.

Measurement errors broaden the range of possible trajectories. Thus we draw final conclusions from the density distribution of possible trajectories. For each star, we perform 10^6 Monte Carlo trajectory calculations assuming that measurement errors are normally distributed. We generate correlated normal distributions for parallax, μ_α, μ_δ using the *Gaia* correlation matrix and a Cholesky decomposition. A ± 0.5 kpc uncertainty in solar position or a ± 10 km s^{-1} uncertainty in circular velocity yield negligible ± 0.5 kpc changes in Galactic plane crossing location and ± 0.2 Myr changes in flight times. Thus we set the solar position and circular velocity error to zero for simplicity. Distance and proper motion are the two dominant sources of uncertainty. We then measure the density of simulated trajectories as they cross the Galactic disk plane.

We evaluate likelihood of origin based on the 0.3173 (1σ), 0.0455 (2σ), and 0.0027 (3σ) thresholds of the trajectory distribution at the Galactic plane. This approach is valid for testing the origin of unbound stars that cross the Galactic plane only once, or bound stars with lifetimes less than their orbital turn-around time; this approach is invalid for long-lived stars that cross the plane more than once. The measurements provide trajectory constraints for about half of the sample, namely for the stars with $R < 60$ kpc.

3.3. Large Magellanic Cloud

Our northern hemisphere sample of stars is poorly suited to test the Large Magellanic Cloud origin hypothesis, which predicts a monopole of unbound stars in the southern sky (Boubert & Evans 2016; Boubert et al. 2017). Nearly all of our stars must pass *through* the disk of the Milky Way to reach the Large Magellanic Cloud in the south. A better test is provided by the southern hemisphere star HE 0437−5439 (Edelmann et al. 2005): its trajectory points from the Large Magellanic Cloud (Erkal et al. 2018) and its unbound velocity possibly requires dynamical interaction with an intermediate mass black hole (Gualandris & Portegies Zwart 2007).

3.4. Ejection Velocity

The ejection velocity required to explain the present position and motion of our stars provides another constraint on their origin. In the absence of an MBH, the speed limit for ejection from a stellar binary is set by the finite sizes of the stars (Leonard 1991). The orbital velocity of an equal-mass pair of stars separated by their radii is equal to the escape velocity from the surface of the stars. Because stars on the main sequence have a quasi-linear relation between mass and radius, most stars in the Milky Way share a common escape velocity from their surface of about 600 km s^{-1}. To achieve higher binary orbital speeds, main-sequence stars would have to orbit inside each other, which is impossible. A 600 km s^{-1} speed limit is optimistic; the speed can only be lower if mass transfer, tidal heating, or binary evolution are taken into account (e.g., Fregeau et al. 2004; Renzo et al. 2018).

Chaining together dynamical and supernova ejections can theoretically yield a higher velocity (Pflamm-Altenburg & Kroupa 2010), but the observable rate of such events is reduced by the joint probability of dynamically ejecting a binary and then disrupting it through a supernova explosion at maximum velocity in the same direction. We estimate that the Galactic center ejection rate is orders of magnitude larger at >600 km s^{-1} speeds (Brown et al. 2009).

The ejection velocities required for the fastest stars in the HVS Survey exceed 600 km s^{-1}. Thus the ejection velocities demand a Galactic center origin. For stars near Galactic escape velocity, however, there is finite region of the Milky Way disk where the stars can be ejected at <600 km s^{-1}. The region is set by the Milky Way gravitational potential and the rotation of the Milky Way disk: the ejection velocity minimum is located in the outer disk, at the position where the disk rotation vector points in the direction of ejection (Bromley et al. 2009). Convolved with the power-law distribution of runaway ejection velocities (Portegies Zwart 2000; Perets & Subr 2012; Renzo et al. 2018), the most probable disk runaway origin location is this region of minimum ejection velocity. We mark the minimum disk ejection velocity region for each star in Figure 2 with a red ellipse.

4. Constraints on Origin

We identify three classes of objects with distinct but overlapping velocity distributions in our sample: (1) Galactic

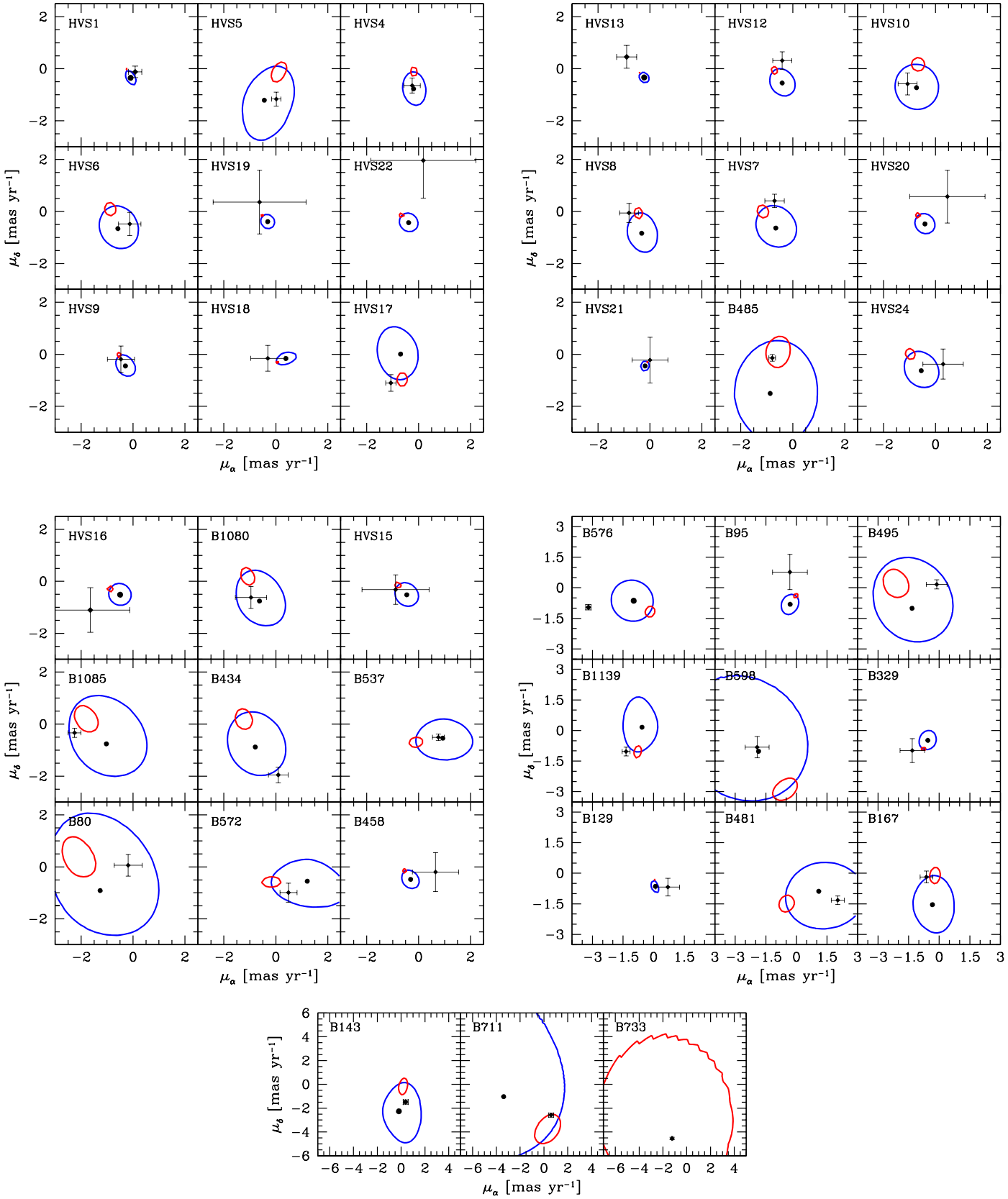

Figure 2. Proper motion measurements and trajectories through the Milky Way. Panels are ordered by decreasing $v_{\rm rf}$, except for the final panel for the three nearest stars. The blue ellipse is the locus of proper motions with trajectories that pass within 20 kpc of the Galactic center, the edge of the Milky Way disk. The small red ellipse is the locus of proper motions within 6 kpc of the point of minimum Galactic disk ejection velocity. A Galactic center trajectory is marked by the black dot.

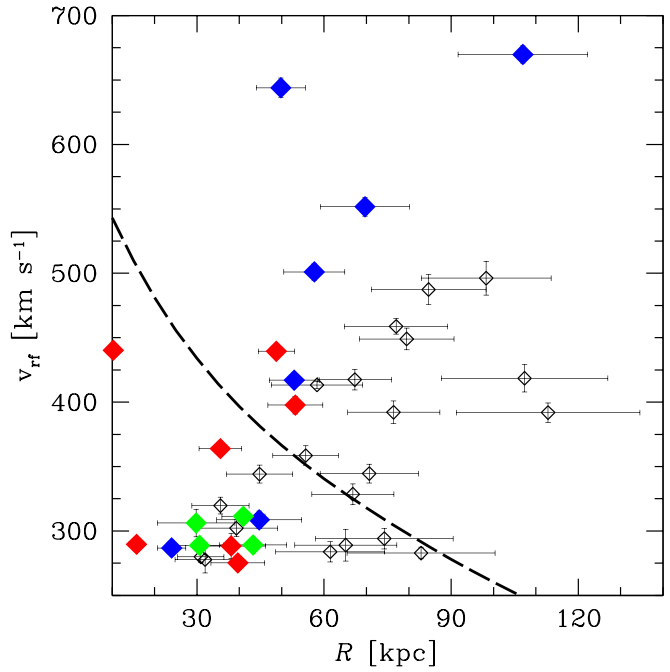

Figure 3. Distribution of v_{rf} vs. Galactocentric radial distance R for the 39 velocity outliers with *Gaia* measurements. Dashed line is Galactic escape velocity in our gravitational potential model (Kenyon et al. 2014). Symbol color indicates probable origin: Galactic center (blue), Galactic disk (red), Galactic halo (green), and ambiguous (empty).

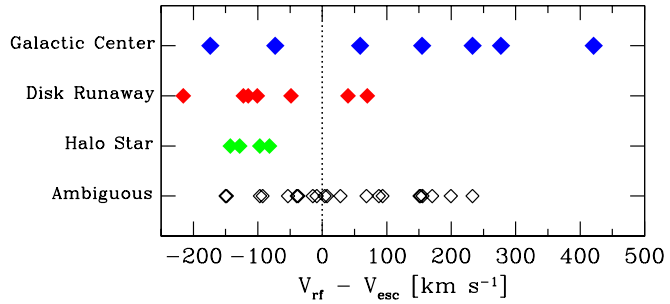

Figure 4. Probable origin, on the basis of trajectory and velocity, plotted relative to Galactic escape velocity.

center HVSs, (2) Galactic disk runaways, and (3) Galactic halo stars. Figures 3 and 4 summarize the results. We discuss the results in terms of v_{rf}, the heliocentric radial velocity transformed to the Galactic frame, because it is the largest component of velocity and the most accurately measured. Figure 3 plots v_{rf} versus Galactic radial distance R. The dashed line is the Galactic escape velocity curve, and symbol color indicates the likely origin of each star. Figure 4 groups the origins together and plots them relative to Galactic escape velocity, v_{rf}–v_{esc}. A total of 18 objects have robust constraints. Table 2 lists the constraints for the full sample, discussed below.

4.1. Galactic Center HVSs

A Galactic center origin is statistically preferred for all of the fastest stars with $v_{rf} > +500\,\mathrm{km\,s^{-1}}$ (HVS1, HVS4, HVS5, and HVS6). The trajectories currently provide 2σ constraints. The velocity itself provides an additional physical constraint for the unbound stars: the minimum Galactic disk ejection

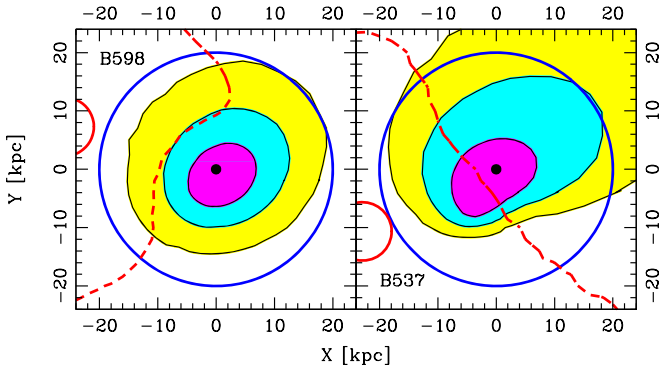

Figure 5. Density of simulated trajectories (magenta region = 1σ, cyan region = 2σ, yellow region = 3σ) where bound HVS candidates B537 and B598 cross the Galactic plane, in Cartesian coordinates. The Galactic center (black dot) is the origin most consistent with the measurements. Trajectories from the region of minimum Galactic disk ejection velocity (solid red lines) are excluded at 3σ confidence; however, 500 km s^{-1} Galactic disk ejections (dashed red lines) are allowed.

velocity is comparable to the escape velocity from the surface of the stars, a severe challenge to disk ejection. We identify seven probable Galactic center HVS ejections.

Two bound stars, B537 and B598, have trajectories that point directly from the Galactic center, and reject the Galactic disk origin hypothesis at $>3\sigma$ significance. To better understand these objects, Figure 5 plots the probability contours where these two objects cross the Galactic plane in Cartesian coordinates. The solid red lines in Figure 5 mark the regions of minimum Galactic disk ejection velocity, excluded at 3σ confidence. The dashed red lines in Figure 5 mark the locus of trajectories with 500 km s^{-1} Galactic disk ejection velocities. Thus it is possible that B537 and B598 are high speed Galactic disk ejections. A factor of 2 improvement in proper motion error would exclude this possibility for B598. It is also possible that B537 and B598 are halo stars on very radial orbits. High resolution spectroscopy can determine whether these are metal-poor halo stars or main-sequence B stars.

Extrapolating these results to the unconstrained half of the sample, we expect that about half of the unbound stars in the HVS Survey are Galactic center ejections. Brown et al. (2014) thus overestimate the number of Galactic center ejections by a factor of two. The implication is that, if HVSs are ejected continuously and isotropically, there are about 50 unbound 2.5–4 $M_\odot$ HVSs over the entire sky to 100 kpc. We compare this number with the theoretical predictions of Zhang et al. (2013). The models that best match the observed distribution of S-stars in the Galactic center and unbound stars in the Galactic halo predict about 10–30 unbound 3–4 $M_\odot$ HVSs over the entire sky. Our revised number of unbound HVSs from the Galactic center is thus in better agreement with theoretical ejection calculations for the MBH ejection scenario.

4.2. Disk Runaways

We estimate the likelihood of Galactic disk origin by averaging the trajectory density over a 5 kpc radius region centered on the position of minimum Galactic disk ejection velocity. This metric can be pessimistic for the nearest bound objects, but it is well-matched to the average distance and proper motion errors of the sample. We identify seven disk runaways with trajectories inconsistent with the Galactic center

Table 2
Constraints on Origin

ID	v_{rf} (km s^{-1})	R (kpc)	$v_{rf}-v_{esc}$ (km s^{-1})	$p_{GC\ HVS}$	$p_{Disk\ Runaway}$
HVS1	669.8 ± 6.6	106.9 ± 15.3	421	0.41959	0.13256
HVS5	644.0 ± 7.5	49.8 ± 5.8	277	0.02566	0.00234
HVS4	551.7 ± 7.3	69.7 ± 10.5	233	0.80644	0.02091
HVS6	501.1 ± 6.3	57.7 ± 7.2	155	0.60588	0.08691
HVS19	496.2 ± 13.1	98.3 ± 15.3	233	0.84863	0.72447
HVS22	487.4 ± 11.5	84.7 ± 13.5	199	0.06899	0.06631
HVS9	458.8 ± 6.1	77.0 ± 12.2	156	1.00000	0.59219
HVS18	449.0 ± 8.5	79.5 ± 11.1	151	0.79264	0.93030
B733	440.3 ± 2.3	10.2 ± 1.2	−101	0.00000	0.00016
HVS17	439.5 ± 4.6	48.7 ± 4.3	70	0.00036	0.07498
HVS13	418.5 ± 10.8	107.3 ± 19.6	170	0.12816	0.84341
HVS12	417.4 ± 8.1	67.2 ± 8.7	94	0.06419	0.36458
HVS10	417.0 ± 4.6	53.0 ± 5.9	59	0.92961	0.10883
HVS8	413.3 ± 2.6	58.3 ± 10.8	69	0.43309	0.52037
HVS7	397.7 ± 6.8	53.2 ± 6.5	40	0.00100	0.11113
HVS20	392.1 ± 8.7	76.4 ± 10.9	88	0.22497	0.16428
HVS21	391.9 ± 7.5	112.9 ± 21.7	153	0.87222	0.54908
B485	363.9 ± 4.8	35.5 ± 5.0	−48	0.00000	0.28713
HVS24	358.6 ± 7.6	55.7 ± 7.7	7	0.53504	0.16045
HVS16	344.6 ± 7.3	70.7 ± 11.6	28	0.98818	0.65225
B1080	344.1 ± 6.9	44.8 ± 7.8	−37	1.00000	0.21767
HVS15	328.5 ± 8.1	66.8 ± 9.7	4	1.00000	0.73678
B1085	319.6 ± 6.5	35.5 ± 6.8	−93	0.22286	0.01703
B434	311.4 ± 2.9	41.0 ± 5.1	−82	0.00155	0.00000
B537	308.6 ± 6.9	44.7 ± 10.0	−73	0.72596	0.00000
B080	306.2 ± 10.7	29.8 ± 9.1	−128	0.00036	0.02590
B572	302.1 ± 6.5	39.3 ± 9.7	−97	0.16757	0.00489
B458	294.1 ± 7.9	74.2 ± 16.3	−15	0.46156	0.13478
B711	289.6 ± 5.4	15.7 ± 1.9	−216	0.00000	0.04737
B576	289.1 ± 2.4	43.2 ± 7.9	−97	0.02239	0.00000
B095	289.1 ± 12.3	65.1 ± 12.0	−40	0.41893	0.97142
B495	288.9 ± 4.6	30.6 ± 5.6	−142	0.00000	0.00243
B1139	288.3 ± 9.7	38.1 ± 8.1	−115	0.00000	0.02608
B598	286.8 ± 5.7	24.0 ± 3.3	−174	0.93866	0.00000
B329	283.9 ± 7.9	61.4 ± 12.8	−53	1.00000	0.41425
B129	282.8 ± 4.5	82.9 ± 17.5	−9	0.21733	0.02988
B143	279.9 ± 4.4	30.9 ± 5.5	−150	0.02091	0.00000
B481	277.8 ± 10.4	31.9 ± 7.1	−148	0.36545	0.00000
B167	275.2 ± 4.3	39.7 ± 6.3	−123	0.00000	0.47101

hypothesis at $\geqslant 3\sigma$ significance, and statistically consistent with a Galactic disk ejection.

Disk runaways and Galactic center HVSs have comparable frequency at speeds around the Galactic escape velocity (Figure 4). The fastest disk runaways have $v_{rf}-v_{esc} \simeq +100$ km s^{-1}. However, most disk runaways are bound.

Interestingly, the two unbound disk runaways are spectroscopically unusual. HVS7 and HVS17 are both chemically peculiar B stars (Przybilla et al. 2008c; Brown et al. 2013). HVS7 is 10–100 times underabundant in He and in CNO relative to the Sun, and 100–10,000 time overabundant in iron group and rare-Earth elements (Przybilla et al. 2008c). It is unclear whether abundance patterns are linked to a supernova binary disruption origin, however. The abundance patterns of the unbound runaway B stars HVS7, HVS17, and HD 271791 (Przybilla et al. 2008b) differ significantly. McEvoy et al. (2017) find no correlation in a more detailed abundance analysis of 38 runaway B stars.

The frequency of unbound runaways is linked to their ejection rate. Theoretical ejection models predict a power-law distribution of ejection velocities (Portegies Zwart 2000; Perets & Subr 2012; Renzo et al. 2018). In these models, >99% of runaways are launched from the disk with <200 km s^{-1} speeds. Simulated distributions of runaways in the Milky Way therefore predict a flattened spatial distribution of runaways with a scale height comparable to the thick disk (Bromley et al. 2009). We expect that magnitude-limited surveys of less luminous types of stars than B stars will find many more runaways near the disk.

4.3. Halo Stars

Halo stars first appear at $v_{rf} < +300$ km s^{-1} in our sample. There are four bound objects with trajectories that significantly reject both Galactic center and Galactic disk origins, and which cross the disk in the direction opposite Galactic rotation. These stars are likely halo stars, presumably hot blue horizontal branch stars with temperatures and surface gravities similar to main-sequence B stars. The number of halo stars is consistent with the number of $-300 < v_{rf} < -275$ km s^{-1} negative velocity outliers in the HVS Survey. At even lower $v_{rf} < 250$ km s^{-1}

velocities, halo stars completely dominate the HVS Survey (Brown et al. 2014).

Indeed, the *Gaia* measurements show that 94% of previously claimed unbound stars are likely bound halo stars (Boubert et al. 2018). Searches targeting high velocity stars in *Gaia* (Hattori et al. 2018a; Marchetti et al. 2018) predominantly find low-mass, metal-poor stars moving in equal numbers toward and away from the Sun; in other words, halo stars.

5. Conclusions

Gaia proper motions enable distinction between true Galactic center HVSs and other high velocity stars. We examine the probable origin for B-type stars from the HVS Survey. Eighteen objects have robust constraints. Halo stars dominate the sample at bound speeds, $v_{\rm rf}-v_{\rm esc} < -100\,{\rm km\ s^{-1}}$. We identify seven disk runaways with trajectories that significantly reject the Galactic center hypothesis. The fastest disk runaways have $v_{\rm rf}-v_{\rm esc} \simeq +100\ {\rm km\ s^{-1}}$, but the majority are bound. We identify seven probable Galactic center HVS ejections. The Galactic center ejections dominate the sample at speeds significantly above Galactic escape velocity.

A clean sample of HVSs is important for constraining the Galactic center ejection mechanism. With a sample of 50 HVSs, for example, discrimination between a single and a binary MBH ejection scenario might be possible (Sesana et al. 2007). Different MBH ejection mechanisms predict different spatial distributions of HVSs on the sky (Levin 2006; Abadi et al. 2009; Zhang et al. 2013; Boubert & Evans 2016; Kenyon et al. 2018). These distributions can be tested with larger samples of HVSs.

A well-defined sample of HVSs will also enable measurement of the ejection rate of stars encountering the MBH. Tidal disruption events may be closely related to the encounters that produce HVSs (Bromley et al. 2012).

Gaia end-of-mission proper motion errors should improve by a factor of 3. There are a dozen objects in our sample with 1–2σ trajectory constraints that will have $>3\sigma$ constraints in only a few years. For the faintest stars, however, *Gaia* cannot compete with pointed observations. Next generation missions like the proposed *Theia* mission (Theia Collaboration et al. 2017) are needed to measure HVS proper motions with uncertainties significantly below 0.1 mas yr^{-1}.

With uncertainties below 0.1 mas yr^{-1}, HVSs become important tools for measuring the Milky Way mass distribution (Gnedin et al. 2005; Yu & Madau 2007). HVSs integrate the gravitational potential from the very center of the Milky Way to its outermost regions. Theorists have proposed measuring the angular momentum of one very nearby HVS (Hattori et al. 2018b) or using the phase space distribution of hundreds of HVSs (Perets et al. 2009; Rossi et al. 2017; Contigiani et al. 2018) to constrain the Milky Way mass distribution. Thus HVSs can complement studies possible now, that use halo star streams (Bonaca & Hogg 2018), globular clusters (Posti & Helmi 2018; Watkins et al. 2018), or dwarf galaxies (Fritz et al. 2018) to constrain the Milky Way dark matter halo. Any deviation of an HVS's trajectory from the Galactic center measures the Milky Way's nonspherical mass distribution, independent of any other technique.

This work has made use of data from the European Space Agency mission *Gaia*, processed by the *Gaia* Data Processing and Analysis Consortium (DPAC). Funding for the DPAC has been provided by national institutions, in particular, the institutions participating in the *Gaia* Multilateral Agreement. This research has made use of NASA's Astrophysics Data System. This research was supported in part by the Smithsonian Institution.

Facility: Gaia.

ORCID iDs

Warren R. Brown https://orcid.org/0000-0002-4462-2341
Scott J. Kenyon https://orcid.org/0000-0003-0214-609X
Margaret J. Geller https://orcid.org/0000-0002-9146-4876

References

Abadi, M. G., Navarro, J. F., & Steinmetz, M. 2009, ApJL, 691, L63
Blaauw, A. 1961, BAN, 15, 265
Bonaca, A., & Hogg, D. W. 2018, ApJ, submitted (arXiv:1804.06854)
Boubert, D., Erkal, D., Evans, N. W., & Izzard, R. G. 2017, MNRAS, 469, 2151
Boubert, D., & Evans, N. W. 2016, ApJL, 825, L6
Boubert, D., Guillochon, J., Hawkins, K., et al. 2018, MNRAS, 479, 2789
Bressan, A., Marigo, P., Girardi, L., et al. 2012, MNRAS, 427, 127
Bromley, B. C., Brown, W. R., Geller, M. J., & Kenyon, S. J. 2009, ApJ, 706, 925
Bromley, B. C., Kenyon, S. J., Geller, M. J., & Brown, W. R. 2012, ApJL, 749, L42
Brown, W. R., Anderson, J., Gnedin, O. Y., et al. 2015, ApJ, 804, 49
Brown, W. R., Cohen, J. G., Geller, M. J., & Kenyon, S. J. 2013, ApJ, 775, 32
Brown, W. R., Geller, M. J., & Kenyon, S. J. 2009, ApJ, 690, 1639
Brown, W. R., Geller, M. J., & Kenyon, S. J. 2012, ApJ, 751, 55
Brown, W. R., Geller, M. J., & Kenyon, S. J. 2014, ApJ, 787, 89
Brown, W. R., Geller, M. J., Kenyon, S. J., & Kurtz, M. J. 2005, ApJL, 622, L33
Brown, W. R., Geller, M. J., Kenyon, S. J., & Kurtz, M. J. 2006, ApJL, 640, L35
Brown, W. R., Geller, M. J., Kenyon, S. J., Kurtz, M. J., & Bromley, B. C. 2007a, ApJ, 660, 311
Brown, W. R., Geller, M. J., Kenyon, S. J., Kurtz, M. J., & Bromley, B. C. 2007b, ApJ, 671, 1708
Camarillo, T., Mathur, V., Mitchell, T., & Ratra, B. 2018, PASP, 130, 024101
Contigiani, O., Rossi, E. M., & Marchetti, T. 2018, MNRAS, submitted (arXiv:1807.04468)
Edelmann, H., Napiwotzki, R., Heber, U., Christlieb, N., & Reimers, D. 2005, ApJL, 634, L181
Erkal, D., Boubert, D., Gualandris, A., Evans, N. W., & Antonini, F. 2018, MNRAS, submitted (arXiv:1804.10197)
Fregeau, J. M., Cheung, P., Portegies Zwart, S. F., & Rasio, F. A. 2004, MNRAS, 352, 1
Fritz, T. K., Battaglia, G., Pawlowski, M. S., et al. 2018, A&A, in press (arXiv:1805.00908)
Gaia Collaboration, Brown, A. G. A., Vallenari, A., et al. 2018a, A&A, 616, A1
Gaia Collaboration, Helmi, A., van Leeuwen, F., et al. 2018b, A&A, 616, A12
Geier, S., Fürst, F., Ziegerer, E., et al. 2015, Sci, 347, 1126
Girardi, L., Grebel, E. K., Odenkirchen, M., & Chiosi, C. 2004, A&A, 422, 205
Gnedin, O. Y., Gould, A., Miralda-Escudé, J., & Zentner, A. R. 2005, ApJ, 634, 344
Greenstein, J. L., & Sargent, A. I. 1974, ApJS, 28, 157
Gualandris, A., & Portegies Zwart, S. 2007, MNRAS, 376, L29
Hattori, K., Valluri, M., Bell, E. F., & Roederer, I. U. 2018a, ApJ, submitted (arXiv:1805.03194)
Hattori, K., Valluri, M., & Castro, N. 2018b, ApJ, submitted (arXiv:1804.08590)
Heber, U., Edelmann, H., Napiwotzki, R., Altmann, M., & Scholz, R.-D. 2008, A&A, 483, L21
Hills, J. G. 1988, Natur, 331, 687
Hirsch, H. A., Heber, U., O'Toole, S. J., & Bresolin, F. 2005, A&A, 444, L61
Justham, S., Wolf, C., Podsiadlowski, P., & Han, Z. 2009, A&A, 493, 1081
Kenyon, S. J., Bromley, B. C., Brown, W. R., & Geller, M. J. 2014, ApJ, 793, 122
Kenyon, S. J., Bromley, B. C., Brown, W. R., & Geller, M. J. 2018, ApJ, 864, 130
Kenyon, S. J., Bromley, B. C., Geller, M. J., & Brown, W. R. 2008, ApJ, 680, 312
Kollmeier, J. A., & Gould, A. 2007, ApJ, 664, 343

Leonard, P. J. T. 1991, AJ, 101, 562
Levin, Y. 2006, ApJ, 653, 1203
Lindegren, L., Hernandez, J., Bombrun, A., et al. 2018, A&A, 616, A2
Marchetti, T., Rossi, E. M., & Brown, A. G. A. 2018, MNRAS, in press (doi:10.1093/mnras/sty2592)
Marigo, P., Girardi, L., Bressan, A., et al. 2008, A&A, 482, 883
McEvoy, C. M., Dufton, P. L., Smoker, J. V., et al. 2017, ApJ, 842, 32
Monari, G., Famaey, B., Carrillo, I., et al. 2018, A&A, 616, L9
Perets, H. B., & Subr, L. 2012, ApJ, 751, 133
Perets, H. B., Wu, X., Zhao, H. S., et al. 2009, ApJ, 697, 2096
Pflamm-Altenburg, J., & Kroupa, P. 2010, MNRAS, 404, 1564
Portegies Zwart, S. F. 2000, ApJ, 544, 437
Posti, L., & Helmi, A. 2018, A&A, 615, A70
Poveda, A., Ruiz, J., & Allen, C. 1967, BOTT, 4, 86
Przybilla, N., Nieva, M. F., Heber, U., et al. 2008a, A&A, 480, L37
Przybilla, N., Nieva, M. F., Heber, U., & Butler, K. 2008b, ApJL, 684, L103
Przybilla, N., Nieva, M. F., Tillich, A., et al. 2008c, A&A, 488, L51
Raddi, R., Hollands, M. A., Gänsicke, B. T., et al. 2018, MNRAS, 479, L96
Reid, M. J., Menten, K. M., Brunthaler, A., et al. 2014, ApJ, 783, 130
Renzo, M., Zapartas, E., de Mink, S. E., et al. 2018, A&A, submitted (arXiv:1804.09164)
Rossi, E. M., Marchetti, T., Cacciato, M., Kuiack, M., & Sari, R. 2017, MNRAS, 467, 1844
Schönrich, R., Binney, J., & Dehnen, W. 2010, MNRAS, 403, 1829
Sesana, A., Haardt, F., & Madau, P. 2007, MNRAS, 379, L45
Shen, K. J., Boubert, D., Gänsicke, B. T., et al. 2018, ApJ, 865, 15
Tauris, T. M. 2015, MNRAS, 448, L6
Theia Collaboration, Boehm, C., Krone-Martins, A., et al. 2017, arXiv:1707.01348
Tian, H.-J., Gupta, P., Sesar, B., et al. 2017, ApJS, 232, 4
Vennes, S., Nemeth, P., Kawka, A., et al. 2017, Sci, 357, 680
Wang, B., & Han, Z. 2009, A&A, 508, L27
Watkins, L. L., van der Marel, R. P., Sohn, S. T., & Evans, N. W. 2018, ApJ, submitted (arXiv:1804.11348)
Yu, Q., & Madau, P. 2007, MNRAS, 379, 1293
Zhang, F., Lu, Y., & Yu, Q. 2013, ApJ, 768, 153